Reliability Engineering and System Safety 214 (2021) 107706

Contents lists available at ScienceDirect

Reliability Engineering and System Safety

journal homepage: www.elsevier.com/locate/ress

Effect of environmental modelling and inspection strategy on the optimal design of floating wind turbines

John Marius Hegseth *, Erin E. Bachynski, Bernt J. Leira

NTNU, Department of Marine Technology, 7491 Trondheim, Norway

ARTICLE INFO

Keywords:
Offshore wind energy
Floating wind turbines
Design optimization
Fatigue reliability
Inspection

ABSTRACT

In order to reduce design conservatism and consequently the cost of energy, appropriate and cost-optimal safety factors should be derived, in light of environmental load uncertainties and lifetime costs. In the present work, a linearized dynamic model has been used together with Monte Carlo simulations and a numerical design optimization procedure to evaluate the impact of the description of wind and wave loads on the fatigue reliability and optimal design of a 10 MW spar floating wind turbine. Trade-offs between design costs and inspection costs with different design fatigue factors (DFFs) have also been assessed. The analyses have been performed for a realistic wind park site, where an environmental model has been developed based on hindcast data. Considering stochastic turbulence intensity, wind-wave misalignment, wind directional distribution, and a two-peak wave spectrum reduced the long-term fatigue damage by approximately two-thirds along the fatigue-critical part of the support structure compared to the base model. Re-designing the tower and platform with the full environmental model resulted in 11% reduction in CAPEX. However, due to the applied design optimization procedure, consistent reliability levels were achieved along the tower length, which resulted in important system side effects for the total structural reliability. Trade-offs between CAPEX and OPEX were derived based on a probabilistic fracture mechanics model and reliability updating through inspections. The necessary inspection intervals to achieve the same accumulated reliability after 20 years of operation were identified with different DFFs, and cost-optimal safety factors were computed with different OPEX costs and interest rates.

1. Introduction

Floating wind turbines (FWTs) are considered a promising solution for wind energy harvesting in deep waters, but are currently too expensive to compete with other energy sources. Being a relatively new and immature technology, there is still a large potential for cost reductions through optimization of the FWT structure. For large parts of the system, the design is typically driven by fatigue, where a large number of environmental conditions potentially should be considered in order to evaluate the lifetime loads. Wind and wave loads are highly stochastic, and due to lack of site-specific data, or to limit the computational effort during the design process, uncertainties in the environmental loads are often replaced by safety factors and deterministic design values. Such design values will typically increase the conservatism, which translates into higher costs.

For the wind turbulence, design values from IEC [1] are commonly used when in situ data are not available. The specified design value for turbulence intensity (i.e. the ratio between the standard deviation of the wind speed and its mean) corresponds to the 90% fractile of the mean wind speed-dependent distribution. Colone et al. [2] considered stochastic turbulence for an offshore wind monopile without waves, and found that using the design value resulted in a 13% increase in damage-equivalent loads (DEL) for the mudline fore-aft bending moment compared to results using Monte Carlo simulations (MCS) with stochastic turbulence intensity. Further, using a linear approximation, the wind-induced DEL was shown to be proportional to the wind speed standard deviation for a given mean wind speed and a given SN curve exponent, suggesting that significant reductions in wind-induced fatigue damage can be achieved by reducing the applied turbulence level. The actual effect of turbulence on the fatigue damage for an offshore wind turbine, however, depends on the relative importance of the response from wind and waves, which varies with different wind-wave conditions, wind turbine concepts, and location of the hotspots in the structure. Also, because of the different natural frequencies of a FWT compared to its bottom-fixed counterpart, the effect of the wind modelling may be altered significantly.

* Corresponding author.
E-mail address: jmhegseth@gmail.com (J.M. Hegseth).

https://doi.org/10.1016/j.ress.2021.107706
Received 19 June 2020; Received in revised form 21 December 2020; Accepted 18 April 2021
Available online 27 April 2021

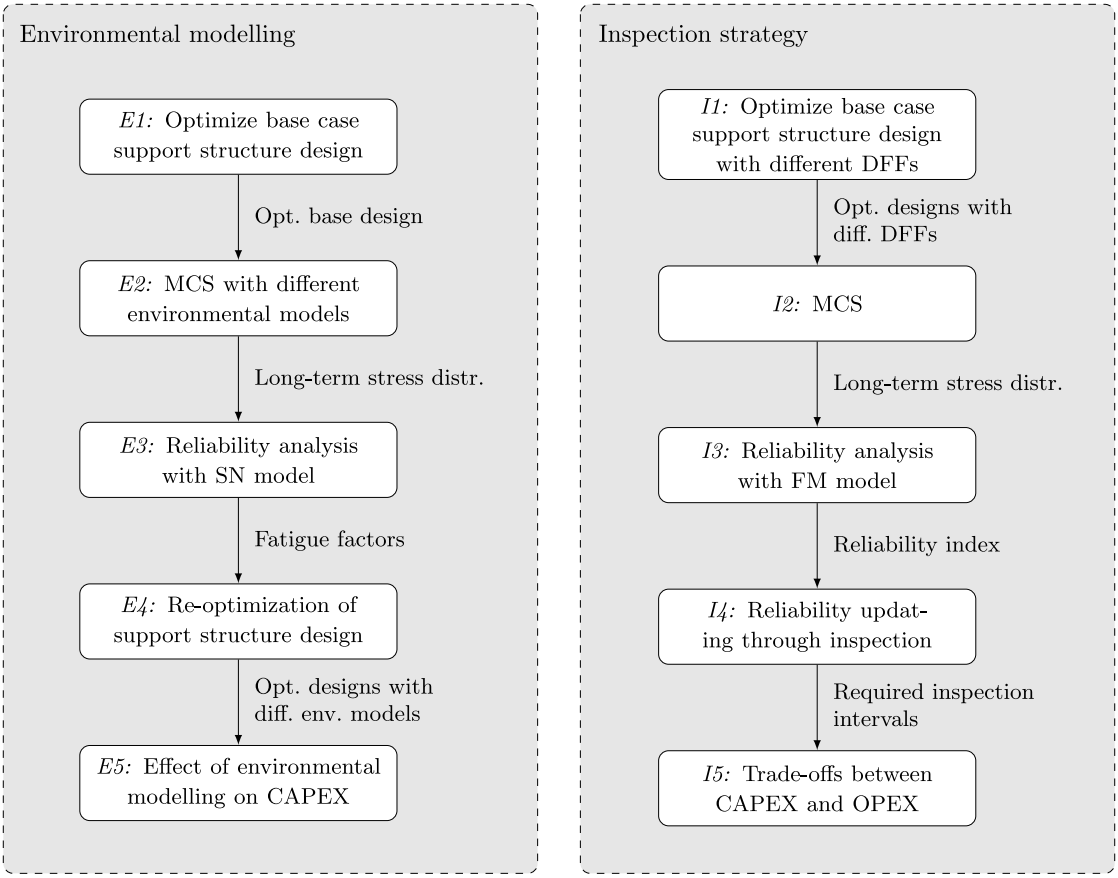

Fig. 1. Analysis flowchart. The numbering of the steps is used as reference in the results section.

Ideally, directional data for the wind and waves should be included in the environmental model during design. The relative wind-wave direction may have a large effect on the response of the structure, and is of particular importance for fatigue [3]. Wind-wave misalignment has been shown to give increased tower base fatigue damage for bottom-fixed offshore wind turbines, due to the low aerodynamic damping for misaligned wave loads. Horn et al. [4] assessed the long-term fatigue reliability of a 10 MW monopile, and found that inclusion of the relative wind-wave direction resulted in a reduced expected lifetime of 7 years compared to co-directional wind and waves. For FWTs, where the natural periods typically are located outside the wave-frequency range, and the tower is sensitive to P-delta effects due to platform pitch, the opposite effect has been observed. Barj et al. [5] studied the effect of wind-wave misalignment on the fatigue and extreme tower base loads for a spar FWT, and although misalignment resulted in significantly increased side-side tower base fatigue loads, the more critical fore-aft loads were slightly reduced. Similar findings were reported by Bachynski et al. [6], for different FWT concepts.

While several studies have assessed the effect of environmental modelling on the reliability of structural components, there are uncertainties related to the resulting impact on the design costs for the system. The potential cost reductions depend on the design-driving limit states for the affected components, which requires re-design of the relevant parts of the structure for a fair comparison.

Although inclusion of more detailed environmental models may increase the estimated fatigue life of the structure and thus reduce the design conservatism, it may increase the complexity or required number of design simulations for a long-term fatigue analysis. Efficient methods to estimate the potential impact of these effects for the specific system under consideration are therefore desirable.

As the goal is to minimize the costs over the lifetime of the system, maintenance costs should ideally be included in the design process. Reliability- and risk-based inspection planning have been used extensively for offshore structures, and more recently, these techniques have also been applied for offshore wind turbine structures [7–10]. Costs related to both design and maintenance are highly dependent on the chosen design fatigue factors (DFFs). Márquez-Domínguez and Sørensen [11] calibrated DFFs for a 2.3 MW offshore wind turbine, and investigated the effect of inspections on the required DFF values. Velarde et al. [12] designed a 10 MW monopile with different DFFs by varying the wall thickness, and found that a DFF of 3 was necessary to achieve the target probability of failure during a service life of 25 years without inspections. Ziegler et al. [13] studied variations in the mass of an 8 MW monopile when the substructure was designed with different DFFs and design lifetimes. For a design lifetime of 25 years, a reduction of the DFF from 3 to 2 was found to save 7% of the steel mass. In order to make decisions on the optimal safety factors and corresponding maintenance strategy, information about the trade-offs between design and inspection costs is needed.

The main objective of the current work is to evaluate the effect of environmental modelling and inspection strategy on the long-term fatigue reliability and associated design costs of a 10 MW spar FWT support structure. While the coupled dynamics of FWTs typically are analysed using nonlinear time-domain analyses, which capture the complex interactions between aerodynamics, hydrodynamics, structural dynamics, and control, such methods become computationally prohibitive for long-term fatigue analyses and design optimization studies, which involve a large number of load cases. The present work therefore uses a computationally efficient linearized global response model, which can be applied in the preliminary design phase. The model has been verified against state-of-the-art nonlinear time-domain analyses with respect to fatigue damage and buckling in the support structure, as well as extreme surge and pitch response, for a 10 MW

spar FWT design in previous work [14]. We found the model to be conservative in general, but reasonably accurate in capturing trends, yielding agreements within 30% for both long-term fatigue damage and short-term extremes, with the exception of the fatigue damage at the tower top. Detailed design would require more accurate nonlinear analyses, incurring a much greater computational cost.

A joint wind-wave distribution for a realistic floating wind park location is established based on hindcast data, and the long term response of the structure is estimated using MCS and a linearized aero-hydro-servo-elastic FWT model. The fatigue reliability for a design lifetime of 20 years is then assessed, considering different environmental models. Based on the results, equivalent fatigue factors are established, and the support structure is re-designed to evaluate the impact of the environmental modelling on the design costs, using a numerical design optimization procedure. Trade-offs between CAPEX and OPEX are assessed by optimizing the design of the support structure with different DFFs, where the fatigue reliability and inspection schedules are established based on probabilistic fracture mechanics (FM). Cost-optimal safety factors are then derived, considering the lifetime costs related to design and inspection of the support structure. The workflow of the present study is summarized in Fig. 1.

2. FWT model

The considered system is a 10 MW spar FWT with catenary mooring, with the rotor design taken from the DTU 10 MW reference wind turbine [15]. The steel hull is partially filled with concrete ballast to achieve the correct draft, using a ballast density of 2600 kg/m^3. The interface with the tower is located 10 m above the still water line (SWL), while the hub height is 119 m above the SWL. An overview of the FWT system, including the mooring system layout, is shown in Fig. 2.

2.1. Linearized system formulation

The system is linearized to obtain the equations of motion, which are solved in the frequency domain. The linearized system considers perturbations in the state and input variables, $\mathbf{x}$ and $\mathbf{u}$ respectively, about the operational point:

$$\mathbf{x} = \mathbf{x_0} + \Delta\mathbf{x}, \quad \mathbf{u} = \mathbf{u_0} + \Delta\mathbf{u}. \tag{1}$$

The state variables which describe the structural responses are outlined in greater detail in Section 2.2. The dynamic equations of motion are then expressed as

$$\Delta\dot{\mathbf{x}} = \mathbf{A}\Delta\mathbf{x} + \mathbf{B}\Delta\mathbf{u}, \tag{2}$$

where $\mathbf{A}$ is the state matrix, which can be found from the total mass ($\mathbf{M}$), stiffness ($\mathbf{K}$), and damping ($\mathbf{D}$) matrices for the system

$$\mathbf{A} = \begin{bmatrix} \mathbf{0} & \mathbf{I} \\ -\mathbf{M}^{-1}\mathbf{K} & -\mathbf{M}^{-1}\mathbf{D} \end{bmatrix}. \tag{3}$$

$\mathbf{B}$ is the input matrix, which describes how the external inputs influence the state variables.

For each wind-wave condition, the operational point for the system is found from equilibrium considerations when the system is subjected to the mean environmental loads. In addition to the mean aerodynamic loads on the rotor, the static component of the aerodynamic drag force on the tower is included.

2.2. Structural model

The numerical FWT model is based on the model presented by Hegseth et al. [14], but with an extended number of structural degrees-of-freedom (DOFs). The present model includes seven DOFs, namely rotor speed, surge, sway, roll, pitch, and the 1st fore-aft and side-side support structure bending modes. The heave and yaw

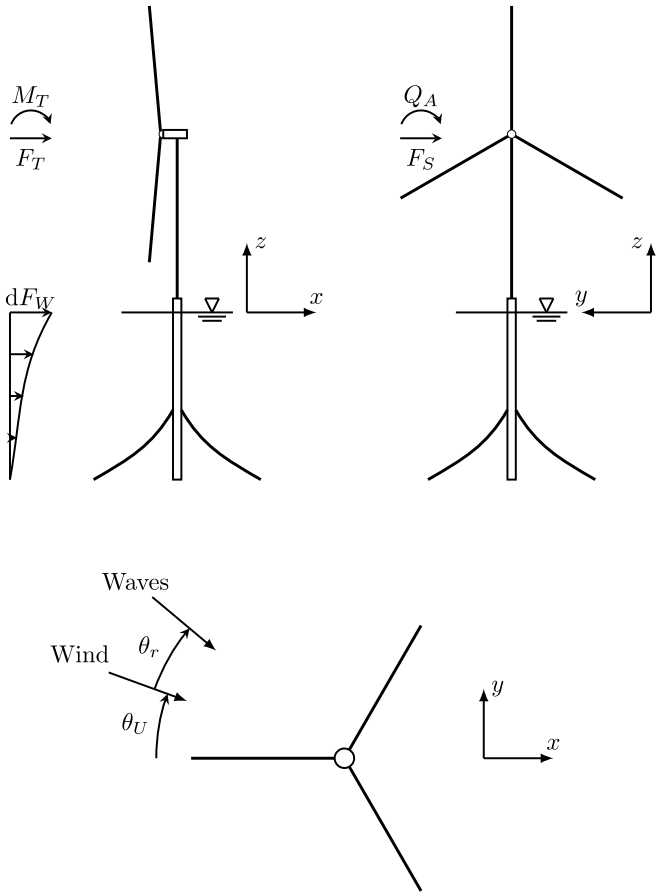

Fig. 2. Overview of the FWT system.

responses are found to have little effect on the support structure fatigue and extreme loads for the considered FWT system, and are therefore neglected. The equations of motion for the support structure DOFs are derived using generalized displacements similar to Hegseth and Bachynski [16], but using a flexible hull. Hydrodynamic excitation loads are found from MacCamy–Fuchs theory [17], while the added mass is based on analytical 2D coefficients. Radiation damping is neglected, while viscous damping is computed using stochastic linearization of the drag term in Morison's equation.

The six support structure DOFs are gathered in the vector $\boldsymbol{\xi} = \begin{bmatrix}\xi_1 & \xi_2 & \xi_4 & \xi_5 & \xi_7 & \xi_8\end{bmatrix}^\top$, while the rotor speed, $\dot{\varphi}$, is described by a single-DOF drivetrain model, and thus only considers the rigid body dynamics of the shaft. The structural state vector is thus written as

$$\mathbf{x}_s = \begin{bmatrix}\boldsymbol{\xi}^\top & \dot{\boldsymbol{\xi}}^\top & \dot{\varphi}\end{bmatrix}^\top. \tag{4}$$

The inputs to the structural system consist of outputs from the control system and disturbances due to environmental loads, which are separated in two different vectors $\mathbf{u}_{sc}$ and $\mathbf{u}_{sd}$. The control input vector is written as

$$\mathbf{u}_{sc} = \begin{bmatrix}Q_G & \theta\end{bmatrix}^\top, \tag{5}$$

where Q_G is the generator torque, and θ is the collective blade pitch angle, which are found from the control system model.

Wind loads on the rotor are derived from linearized BEM theory with the incoming wind field described by the Kaimal spectrum and an exponential coherence function for the longitudinal wind velocity component [1]. The blades are considered rigid in the model, and the aerodynamic forces on the rotor are applied as resultant loads at the tower top. The incoming wind is described by a rotor effective wind

Table 1
Mooring system properties.

Parameter	Value	Unit
Radius to anchors	1497.2	m
Unstretched mooring line length	1433.0	m
Equivalent mooring line mass density	125.4	kg/m
Equivalent mooring line axial stiffness	5.90×10^8	N
Fairlead depth below SWL	50.0	m

Table 2
Applied values for control system parameters.

Parameter	Value	Unit
$k_{i,Q}$	0.153×10^8	Nm s/rad
$k_{p,Q}$	0.684×10^8	Nm/rad
$k_{i,\theta}$	0.901×10^{-2}	rad/rad
$k_{p,\theta}$	0.687	rad s/rad
k_f	−0.112	s/m
$\omega_{c,f}$	0.197	rad/s

speed for each of the four resultant forces in Fig. 2, as described in detail by Hegseth et al. [14].

The disturbance vector is expressed as

$$\mathbf{u}_{sd} = \begin{bmatrix} v_{F_T} & v_{M_T} & v_{Q_A} & v_{F_S} & F_{W,1} & F_{W,2} & F_{W,4} & F_{W,5} & F_{W,7} & F_{W,8} \end{bmatrix}^\top, \tag{6}$$

where v_{F_T}, v_{M_T}, v_{Q_A}, and v_{F_S} are the effective wind speeds for thrust, tilting moment, aerodynamic torque, and sideways force, respectively. $F_{W,n}$ represents the generalized wave excitation force in support structure DOF number n.

The mooring system, described in Table 1, consists of three catenary lines spread symmetrically about the vertical axis. For simplicity, the bridle lines are removed, and lines with constant properties are used all the way up to the fairleads.

2.3. Control system

The linear control system consists of two main parts: a generator-torque controller and a collective blade-pitch controller, which work independently in below-rated and above-rated wind speeds, respectively. Below rated wind speed, the generator torque is varied using a PI controller to maintain an optimal tip-speed ratio at the mean wind speed. Above rated wind speed, the generator torque is kept constant at the rated torque, and a gain-scheduled PI controller is used to modify the collective blade pitch angle. Nacelle velocity feedback is included for the blade-pitch controller, and is implemented by modifying the rotor speed Ref. [18]. To avoid controller action on wave-frequency motions, the nacelle velocity signal is passed through a first order low-pass filter with corner frequency $\omega_{c,f}$ to remove wave-frequency components before it is fed back to the blade-pitch controller.

The applied control system parameters are shown in Table 2. Here, $k_{i,Q}$ and $k_{p,Q}$ are the integral and proportional gains of the torque controller, $k_{i,\theta}$ and $k_{p,\theta}$ are the integral and proportional gains of the blade-pitch controller, and k_f is the nacelle velocity feedback gain. The values for the torque controller are taken from the original DTU 10 MW turbine, while the PI gains for the blade pitch controller, as well as the nacelle velocity feedback gain and corner frequency, are based on optimized values identified by Hegseth et al. [19].

2.4. Response to stochastic input

After establishing the coupled linearized model, it is transformed to the frequency domain. Using the transfer matrix between inputs and outputs for a frequency ω, $\mathbf{H}(\omega)$, the cross-spectral density matrix of the response vector $\mathbf{y}$ can be calculated from

$$\mathbf{S}_\mathbf{y}(\omega) = \mathbf{H}(\omega)\mathbf{S}_\mathbf{u}(\omega)\mathbf{H}(\omega)^H, \tag{7}$$

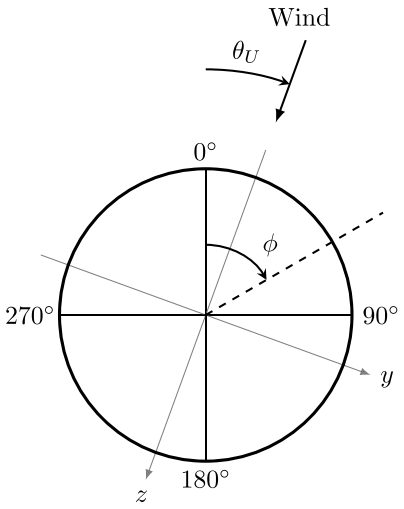

Fig. 3. Coordinate system for stress calculations.

where $(\cdot)^H$ denotes the conjugate transpose [20]. The cross spectral density matrix for the load process, $\mathbf{S}_\mathbf{u}(\omega)$, has the following structure

$$\mathbf{S}_\mathbf{u}(\omega) = \begin{bmatrix} \mathbf{S}_{\text{wind}}(\omega) & \mathbf{0} \\ \mathbf{0} & \mathbf{S}_{\text{wave}}(\omega) \end{bmatrix}, \tag{8}$$

where the off-diagonal terms are zero because the wind and wave processes are assumed to be uncorrelated [21].

The fatigue damage is calculated at selected locations in the tower using the Dirlik method [22], while the extreme response of the support structure is found from upcrossing analysis. We consider one hour to be a typical duration of a stationary wind-wave condition, and use the 1-h most probable maximum value in selected 50-year conditions to represent the extreme design loads. The model has earlier been verified against fully coupled nonlinear time domain simulations in SIMA by Hegseth et al. [14], who found that the linearized model is conservative in general, but reasonably accurate in capturing trends for the support structure response.

2.5. Stress calculations

In the response calculations, the axial stress is calculated for 24 points around the circumference of the tower and hull. The current FWT support structure is axisymmetric, and results from initial analyses showed that the orientation of the mooring system relative to the wind direction had very little effect on the considered stresses. All analyses are therefore run with the same wind direction, and the stress distribution around the circumference is rotated in each wind-wave condition during post-processing to account for the actual wind direction. In all conditions, 0° yaw misalignment is assumed.

The coordinate system used in the stress calculations is shown in Fig. 3. The location along the circumference, ϕ, is defined relative to true north, whereas the local coordinate system for the cross-section follows the wind direction.

Based on the coordinate system in Fig. 3, the total stress in the axial direction at a given point with radius r and angle ϕ, $\sigma_x(\phi)$, is calculated from

$$\sigma_x(\phi) = \frac{N_x}{A} + \frac{M_y}{I_y} r\cos(\phi - \theta_U) + \frac{M_z}{I_z} r\sin(\phi - \theta_U). \tag{9}$$

Here, N_x is the axial force, A is the cross-sectional area, M_y and M_z are bending moments about the local y- and z-axis, respectively, and I_y and I_z are the corresponding second moments of area.

In the fatigue calculations, the nominal stress from the global analysis is multiplied by a stress concentration factor (SCF) to account for

Table 3
Description of metocean parameters for each discrete wind direction.

Parameter	Description	Distribution
U	Mean wind speed at 119 m above SWL	Weibull
H_s	Significant wave height	Weibull
T_p	Spectral peak period	Lognormal
Θ_r	Relative wind-wave direction	von Mises

misalignment between support structure segments. The SCF applied in the present work is taken from Lotsberg [23] and is expressed as

$$\mathrm{SCF} = 1 + 3\frac{\delta}{t_w}\exp\left\{-\frac{0.91L}{\sqrt{(D_w - t_w)t_w}}\right\}, \tag{10}$$

where δ is the misalignment, D_w is the outer diameter, t_w is the wall thickness, and L is the length of the weld, which is taken to be equal to the wall thickness. The misalignment is assumed equal to $0.15t_w$, which is a typical fabrication tolerance for girth welds in offshore structures [23].

3. Environmental description

The description of the wind and wave environment is based on hindcast data from the NORA10 archive, developed by the Norwegian Meteorological Institute [24]. The data are provided for every three hours over a period of 60 years, for a location approximately 25 km west of Norway. The water depth at the location is 250 m.

A joint environmental distribution for wind direction, wind speed, wave height, wave period, and wind-wave misalignment is derived from the hindcast data to have a statistical description of the metocean conditions at the site. No separation between wind sea and swell is made, and the former is considered for the total wave elevation. The joint distribution is denoted $f_{\mathbf{X}_e}$, where

$$\mathbf{X}_e = \left[\Theta_U, U, H_s, T_p, \Theta_r\right]. \tag{11}$$

Here, Θ_U is the wind direction, U is the wind speed at hub height 119 m above the SWL, H_s is the significant wave height, T_p is the spectral peak period, and Θ_r is the relative wind-wave direction. The hindcast data report wind speed at 10 m above SWL, and the hub height wind speed is therefore derived by assuming a power law profile with exponent 0.14 [25].

For the wind direction, 24 discrete sectors are considered, and the marginal distribution is thus expressed as

$$f_{\Theta_U}(\theta_{U,i}) = p(\theta_{U,i}), \quad i = 1, 2, \ldots, 24, \tag{12}$$

where $\theta_{U,i}$ is the midpoint of sector i. The resulting distribution is shown in Fig. 4. For each wind direction, the distributions given in Table 3 are fitted to the mean wind speed, significant wave height, spectral peak period, and relative wind-wave direction.

For simplicity, each of the conditional distributions is assumed to only depend on a single additional parameter, which earlier has been shown to give satisfactory results [26]. Consequently, the environmental joint probability distribution is written

$$f_{\mathbf{X}_e} = f_{\Theta_U} \cdot f_{U|\Theta_U} \cdot f_{H_s|U} \cdot f_{T_p|H_s} \cdot f_{\Theta_r|U}. \tag{13}$$

Conditional distribution parameters, such as mean values, standard deviations, scale and shape parameters etc., are fitted to the data using a least-squares algorithm and the following nonlinear function:

$$c(x) = c_0 + c_1 x^{c_2}. \tag{14}$$

The applied fitting constants are given in the Appendix. In Fig. 5, the hindcast data are compared to results from MCS using the fitted distributions. The largest deviations are observed for the relative wind-wave direction, which is not fully captured by the chosen von Mises distribution conditioned on the wind speed.

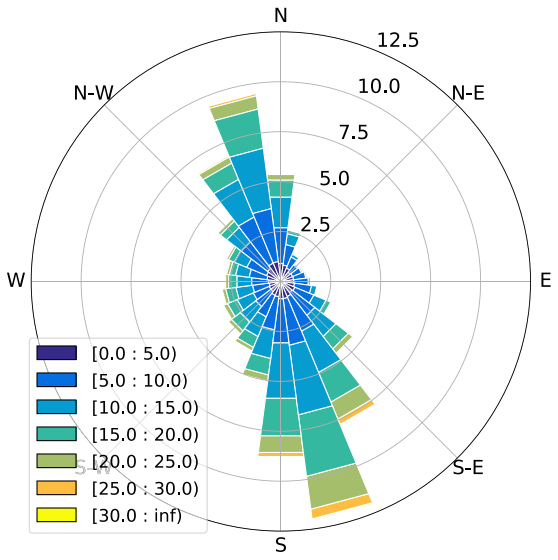

Fig. 4. Distribution of wind directions, 24 sectors. The legend indicates the hub height wind speed.

4. Design optimization problem

To optimize the design of the support structure, a numerical optimization scheme as presented by Hegseth et al. [14] is used. The linearized FWT model is implemented in OpenMDAO [27], which is an open-source framework for multidisciplinary design, analysis, and optimization. The design is then optimized using a gradient-based approach with analytic derivatives computed for the coupled model. The optimization problem is solved using the SNOPT algorithm [28], which uses a sequential quadratic programming (SQP) approach through the pyOptSparse Python interface [29].

To limit the computational effort, a simplified version of the model presented in Section 2 is used in the design optimization. Here, the numerical FWT model considers only 2D response with co-directional wind and waves, and a reduced set of environmental conditions (ECs). The 2D model has four DOFs: surge, pitch, the 1st fore-aft support structure bending mode, and the rotor speed, and the wind and waves are assumed to travel in the positive x-direction in Fig. 2. To include effects of various environmental model uncertainties in the design process, equivalent fatigue factors are developed based on MCS, and these are applied on the fatigue constraints in the optimization.

4.1. Objective function

The objective function used in the present work is the combined cost of the tower and platform, C_{spar} and C_{tower} respectively:

$$f = C_{\text{spar}} + C_{\text{tower}}. \tag{15}$$

The costs consider both material and manufacturing, using the cost models developed by Farkas and Jármai [30]. The cost of the platform (and similarly for the tower) is expressed as

$$C_{\text{spar}} = k_m M_{\text{spar}} + k_f \sum_i T_i, \tag{16}$$

where k_m is the steel cost factor, M_{spar} is the steel mass of the hull, and k_f is the fabrication cost per unit time. T_i is the time spent at the fabrication stage i, expressed as a function of the geometry. The steel cost factor, k_m, is assumed to have a value of 2.7 €/kg, while the ratio between the material and fabrication cost factors, k_m/k_f, is set to 1.0 [30]. The cost of concrete ballast is much lower than the cost of structural steel [31], and is therefore neglected in the current work.

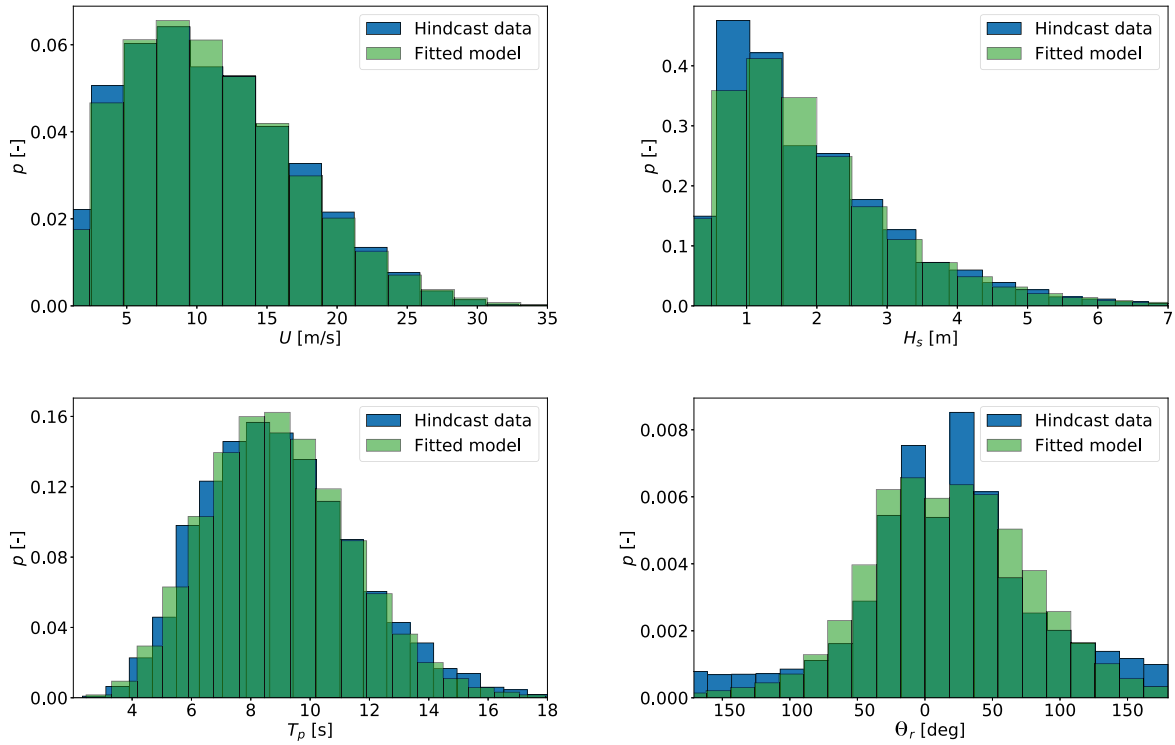

Fig. 5. Comparison of hindcast data with results from MCS using fitted distributions.

4.2. Design variables

Both the platform and tower are discretized into ten sections along the length. For the tower, the diameter and wall thickness at the nodes connecting the sections are set as design variables, while the length of the tower sections is kept fixed to maintain the original hub height. For the platform, the diameter and wall thickness at the nodes, as well as the section lengths, are included. A total of 54 design variables are thus considered in the optimization. The formulation of the optimization problem requires all design variables to be continuous, and the availability of different diameters or wall thicknesses based on e.g. catalogue values is not considered.

The optimization study by Hegseth et al. [14] found that a local minimum existed in both the soft–stiff and stiff–stiff range for the tower design, and the results from the optimization thus depends on the initial starting design. In the present work, only a single initial design is considered, which results in stiff–stiff solutions for the first tower mode.

4.3. Constraints

The fatigue damage at each support structure node is evaluated using an SN curve approach, where the D curve in air from DNV [32] is applied for the tower, and the corresponding curve with cathodic protection is applied for the spar platform. The lifetime of the FWT system is chosen to be 20 years, and the fatigue design constraints are thus expressed as

$$D_{tot} = N_{20} \sum_{i=1}^{N_{EC}} p_i D_i \leq \frac{1.0}{\mathrm{DFF}}, \tag{17}$$

where D_{tot} is the total fatigue damage in 20 years, N_{20} is the number of short-term conditions in 20 years, and D_i is the fatigue damage in condition i. Different DFFs are applied in the present work, as shown in Table 4, where larger safety factors are applied for the platform relative to the tower due to more difficult inspection access. The values in Table 4 correspond to the DFFs for low, normal, and high safety class in the previous DNV standard [33], assuming that the tower is accessible for inspection and repair in dry and clean conditions, while the platform is not.

Table 4
Applied DFFs.

Design	Tower	Platform
'DFF1'	1.0	2.0
'DFF2'	2.0	3.0
'DFF3'	3.0	6.0

Global buckling in the tower is assessed using Eurocode 3 [34], assuming that the tower is stiffened between each section to reduce the buckling length. Buckling of the shell plating in the hull is assessed according to DNV [35], assuming a ring stiffened cylinder with the stiffener design presented by Hegseth et al. [14]. To ensure a smooth transition between the platform and tower, the tower base diameter and wall thickness are set to be equal to the diameter and wall thickness at the platform top. Both fatigue and buckling constraints are aggregated using the Kreisselmeier–Steinhauser (KS) functions [36].

The maximum platform pitch angle in the considered 50-year conditions is limited to 15°. Although the heave response is not included in the model, heave resonance in the wave frequency range is avoided by placing a lower limit of 25 s on the heave natural period. The added mass in heave is approximated as the value for a 3D circular disc with the same diameter as the platform bottom.

The presented model is strictly valid for hull sections with vertical walls, and a maximum taper angle of 10° is therefore applied as a constraint for each section of the platform, to avoid shapes where the physics are not captured correctly. Offset constraints are not considered, as the surge response is mostly governed by the rotor and mooring system design.

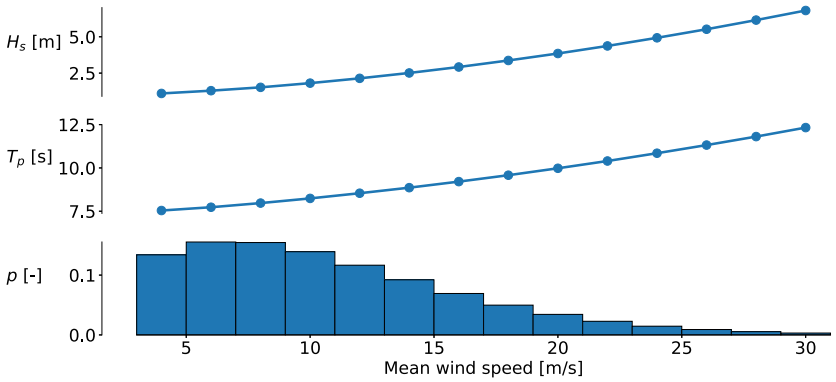

Fig. 6. Significant wave heights, spectral peak periods, and normalized probabilities associated with mean hub height wind speeds applied in the optimization.

Table 5
Environmental conditions for extreme response calculations.

Condition	1	2
Mean wind speed at hub height, U (m/s)	11.0	50.0
Significant wave height, H_s (m)	7.5	15.1
Spectral peak period, T_p (s)	12.0	16.0
Turbulence intensity at hub height, I (-)	0.18	0.12

4.4. Environmental conditions

Fourteen ECs are used to evaluate the lifetime fatigue performance in the optimization. The conditions span mean wind speeds from 4–30 m/s with 2 m/s step, while values for the significant wave height and peak period are chosen such that the resulting long-term response is approximately equivalent to that of a full long-term analysis. The applied parameters are shown in Fig. 6. Only co-directional wind and waves are considered in the numerical optimization process.

Two ECs, described in Table 5, along the 50-year contour surface are selected to evaluate the extreme response, based on results from previous studies on similar FWT designs [14,16]. In EC 1, the mean wind speed is close to the rated speed of the turbine, which gives the maximum thrust force on the rotor. EC 2 represents an extreme wind speed above cut-out, where the turbine is parked and the blades are feathered.

5. Fatigue reliability formulation

The formulation of the probabilistic SN and FM models used in the reliability analysis are described in the following subsections.

5.1. SN approach

The fatigue limit state function at a location ϕ on the circumference of the support structure is expressed as

$$g(t) = \Delta - tN_{3h}\overline{D}(\phi), \tag{18}$$

where Δ is the fatigue damage at failure, t is the time in years, N_{3h} is the number of short-term conditions in a year, and $\overline{D}$ is the expected 3-h fatigue damage. The probability of failure is calculated from

$$P_F(t) = P\left[g(t) \le 0\right], \tag{19}$$

using the first-order reliability method (FORM) [37] by application of the probabilistic analysis software PROBAN [38]. The corresponding reliability index can then be expressed as

$$\beta(t) = -\Phi^{-1}(P_F(t)), \tag{20}$$

where Φ^{-1} is the inverse standard normal cumulative distribution function (CDF).

Because the response characteristics of the structure are highly dependent on the state of the system, the fatigue damage is separated into four groups, as suggested by Horn and Leira [39]:

$$\overline{D}(\phi) = \sum_{i=1}^{4} p_i \overline{D}_i(\phi). \tag{21}$$

Here, p_i and $\overline{D}_i$ are the probability of, and the 3-h expected fatigue damage in, state i, respectively, which points to one of the following wind turbine states:

1. Operational turbine (4–25 m/s)
2. Parked turbine, wind speed below cut-in (< 4 m/s)
3. Parked turbine, wind speed above cut-out (> 25 m/s)
4. Unavailable turbine due to fault

The availability of the turbine is described by the availability parameter α, which is defined here as the duration that the wind turbine is able to produce electricity divided by the total duration spent inside the operational wind speed range. In the present work, the availability is assumed to be 90% [21]. For unavailable conditions, the turbine is assumed to be parked with the collective blade pitch angle fixed at the operational point for the considered mean wind speed. The availability is assumed to be independent of the environmental conditions.

For a given wind-wave condition, the damage in T seconds for a process with mean cycle rate ν is then expressed as

$$D = \frac{\nu T}{K}\left(X_M X_{\mathrm{SCF}}\overline{S}\right)^m \left(t_w / t_{\mathrm{ref}}\right)^{mk}. \tag{22}$$

Here, K is the intercept of the SN curve with the log N axis, X_M and X_{SCF} are uncertainties associated with the dynamic model and SCFs, respectively, and m is the slope of the SN curve. Initial analyses with the present FWT concept showed that there is very little contribution on the resulting fatigue damage from the low-cycle part of the SN curve, suggesting that the high-cycle parameters can be used in the analyses without notable loss of accuracy. A single-slope curve is therefore used in the calculations.

$\overline{S}$ is the equivalent nominal stress range, which can be calculated from the expected value of the stress ranges to the power m:

$$\overline{S} = \left(E\left[S^m\right]\right)^{1/m}. \tag{23}$$

The expected value of S^m is estimated using the Dirlik method [22]:

$$\begin{aligned} E[S^m] &= \int_0^\infty s^m f_S(s)\mathrm{d}s \\ &= (2\sigma_{(\sigma_x)})^m \left(G_1 Q^m \Gamma(1+m) + (\sqrt{2})^m (G_2 R^m + G_3)\Gamma(1+\frac{m}{2})\right), \end{aligned} \tag{24}$$

where Γ is the Gamma function, and $G1$, $G2$, $G3$, Q, and R are empirical parameters. The mean cycle rate is found from the second and fourth order spectral moments:

$$\nu = \frac{1}{2\pi}\sqrt{\frac{m_4}{m_2}}. \tag{25}$$

Table 6
Stochastic variables used in SN model.

Parameter	Distribution	Mean value	Standard deviation
Δ	Lognormal	1.0	0.3
$\log K$	Normal	16.006	0.2
m	Fixed	5.0	–
X_M	Lognormal	1.0	0.1
X_{SCF}	Lognormal	Eq. (10)	0.05
t_{ref}	Fixed	0.025	–
k	Fixed	0.2	–
α	Fixed	0.9	–

Table 7
Stochastic variables used in FM model. Values are given for stresses and crack lengths in MPa and mm, respectively.

Parameter	Distribution	Mean	Standard deviation
m	Fixed	Calibrated	–
$\log C$	Normal	Calibrated	0.22
Y	Normal	1.0	0.05
a_0	Exponential	0.043	0.043
X_M	Lognormal	1.0	0.1
X_{SCF}	Lognormal	Eq. (10)	0.05

The long-term values of $E[S^m]$ and ν are estimated using MCS, where the simulations are run until a coefficient-of-variation (CoV) of less than 0.02 is achieved. The resulting statistical uncertainties in these parameters have small impact on the results, and are therefore neglected in the subsequent reliability analysis.

Uncertainties in the Miner–Palmgren summation (Δ) and SN curve parameters (K, m) are modelled as described by DNV GL [32,40], while typical values from the literature are used for X_M and X_{SCF} [4,8,12]. A summary of the variables are given in Table 6.

5.2. FM approach

To evaluate the effect of inspections on the fatigue reliability, a probabilistic FM model is utilized. Here, the crack growth is estimated from linear-elastic fracture mechanics by assuming that it follows Paris' law:

$$\frac{\mathrm{d}a}{\mathrm{d}N} = C(\Delta K)^m, \tag{26}$$

where a is the crack depth, N is the number of stress cycles, and C and m are material parameters. An initial crack size a_0 is also assumed. ΔK is defined as

$$\Delta K = S\sqrt{\pi a}\, Y. \tag{27}$$

where S is the stress range, and Y is a geometry function. The limit state function is expressed as

$$g(t) = a_c - a(t), \tag{28}$$

where a_c is the critical crack depth, which is set equal to the wall thickness of the structure at the hotspot location. Using Eqs. (26) and (27), the limit state function may be written [41]

$$g(t) = \int_{a_0}^{a_c} \frac{\mathrm{d}a}{Y^m(\sqrt{\pi a})^m} - C(X_M X_{\mathrm{SCF}})^m \sum_{i=1}^{N} S_i^m, \tag{29}$$

where the sum of the stress ranges, which includes stresses from both operational and parked conditions, as described in Section 5.1, can be found from the expected value and the annual cycle rate (ν_y) [40]:

$$\sum_{i=1}^{N} S_i^m = N E[S^m] = \nu_y t E[S^m]. \tag{30}$$

The distributions of Y and a_0, as well as the standard deviation of C, are taken from DNV [40]. The fixed value of m and the mean value of C are found from calibration with the SN model (see Table 7). .

Table 8
Probability of detection curve parameters for eddy current and ultrasonic testing [40].

Parameter	Eddy current	Ultrasonic testing
X_0	0.45	0.41
b	0.9	0.642

The event margin for crack detection during inspection at time t_i is defined as [42]:

$$h(t_i) = \int_{a_0}^{a_d} \frac{\mathrm{d}a}{Y^m(\sqrt{\pi a})^m} - C(X_M X_{\mathrm{SCF}})^m \nu_y t_i E[S^m] \tag{31}$$

where h is negative when a crack is detected, and positive otherwise. The probability of detecting a crack with size a_d is given by the following CDF [40]:

$$P_d(a_d) = 1 - \frac{1}{1 + \left(a_d / X_0\right)^b}, \tag{32}$$

where the distribution parameters X_0 and b are dependent on the inspection conditions. In the present work, inspection by eddy current or equivalent is assumed for welds above the SWL, while ultrasonic testing from the inside is assumed for welds below the SWL [40]. The applied detection parameters are given in Table 8.

To limit the complexity of the reliability updating, all inspections are assumed to result in no crack detection. After k inspections, the probability of failure can thus be found using Bayes theorem [43]:

$$P_{F,up} = P\left[(g \le 0) \mid \bigcap_{i=1}^{k}(h_i > 0)\right] = \frac{P\left[(g \le 0) \bigcap_{i=1}^{k}(h_i > 0)\right]}{P\left[\bigcap_{i=1}^{k}(h_i > 0)\right]} \tag{33}$$

6. Environmental model uncertainties

To assess the importance of different environmental model uncertainties, they are divided into cases which are run separately. The following cases are considered:

- Base case
- Stochastic turbulence
- Wind directional distribution
- Wind-wave misalignment
- Two-peak wave spectrum

The base case considers the stochastic variables given in Table 6, deterministic turbulence intensity, a single wind direction, no wind-wave misalignment, and a JONSWAP spectrum with a peakedness parameter dependent on H_s and T_p for the wave elevation process [21].

If site-specific data on turbulence intensity is unavailable, values from IEC [1] can be used. Here, the design value of the turbulence standard deviation (σ_U) for a normal turbulence model (NTM) is given as

$$\sigma_U = I_{\mathrm{ref}}\,(0.75U + 5.6), \tag{34}$$

where I_{ref} is the reference value of the turbulence intensity, which depends on the site class. Alternatively, the intensity can be described by a two-parameter Weibull distribution with scale parameter β_σ and shape parameter α_σ:

$$\beta_\sigma = I_{\mathrm{ref}}\,(0.75U + 3.3), \quad \alpha_\sigma = 0.27U + 1.4, \tag{35}$$

where the design value in Eq. (34) corresponds to the 90% quantile in this distribution [1].

The impact of stochastic turbulence is assessed by running the long-term analysis with the Weibull distribution described in Eq. (35). In all simulations, medium (class B) turbulence characteristics are assumed.

While the base case assumes that all wind-wave conditions have the same wind direction, the actual wind direction distribution is

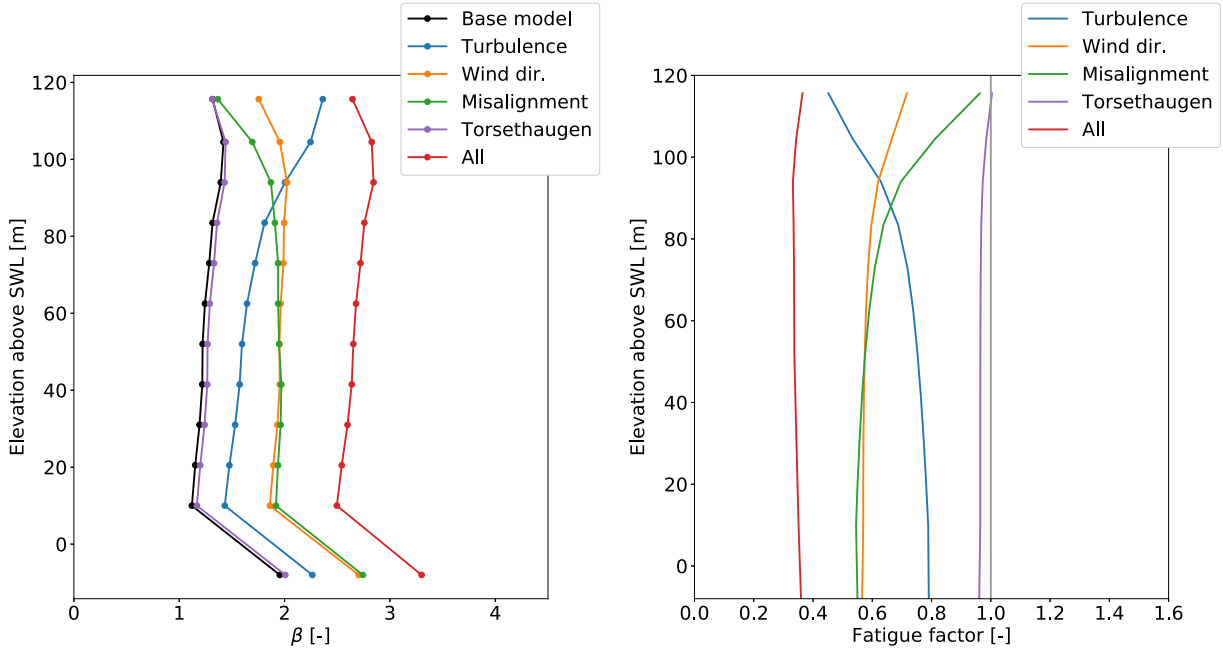

(a) Reliability index for 20 years service life.

(b) Equivalent fatigue factors.

Fig. 7. Effect of environmental modelling on long-term fatigue.

considered here using the discrete distribution with 24 bins given in Eq. (12). The wind and waves are still assumed to be co-directional.

The effect of misalignment is assessed by including the conditional distribution for the relative wind-wave direction, $f_{\Theta_r|U}$, in the environmental model applied in the dynamic analyses.

To account for both wind sea and swell in the analysis, a simplified Torsethaugen spectrum [44] is applied instead of the JONSWAP spectrum. The model takes the significant wave height and the spectral peak period as input parameters, and derives the total wave spectrum from the sum of wind sea and swell. The sea system dominating a particular sea state depends on the value of T_p, relative to the peak period for fully developed seas at the location. In any case, the total wave energy is the same as for the JONSWAP spectrum.

7. Results

The results of the study, presented in the following subsections, are divided into four parts. First, the effect of the environmental modelling on the long-term fatigue is discussed. Subsequently, the resulting impact on the optimized support structure designs is described, where changes in structural dimensions, design-driving limit states, and design costs are discussed. The effect of DFFs on the system reliability and corresponding inspection plan is then assessed. Finally, trade-offs between design costs and inspection costs are presented, and cost-optimal safety factors in a lifetime perspective are discussed.

7.1. Effect of environmental modelling

The resulting equivalent fatigue factors from *E3* with all environmental models described in Section 6, as well as the accumulated reliability indices after 20 years of operation, are presented in Fig. 7. The fatigue factor at a given hotspot for case X is found from the difference in maximum expected circumferential fatigue damage compared to the base case, i.e.,

$$\text{EFF} = \frac{\max\left\{E[\overline{D}_X(\phi)]\right\}}{\max\left\{E[\overline{D}_0(\phi)]\right\}}, \tag{36}$$

where $\overline{D}_0$ is the base case damage. The results are shown for the fatigue-critical parts of the support structure, which consist of the tower and upper part of the platform. For depths below approximately 10 m, shell buckling becomes the design driving constraint, and the differences in fatigue loads do not affect the design process.

The inclusion of swell through a two-peak wave spectrum is found to have small impact on the fatigue reliability for the present support structure, with differences of less than 5% in long-term fatigue damage along the entire length. Significant variations in response between the Torsethaugen and JONSWAP spectra mostly occur in conditions with relatively rare combinations of H_s and T_p, which contribute little to the overall damage estimates.

The effect of turbulence and wind-wave misalignment vary significantly along the length of the structure due to differences in the relative importance of wind and wave response. The tower top response, which is almost exclusively governed by wind loads, is much more affected by the turbulence modelling than the tower base, and vice versa for wind-wave misalignment. This also results in some location-dependent effects when the wind directional distribution is included.

However, the response near the tower top is more sensitive than the lower parts of the structure to the modelling of the rotor-nacelle assembly, which for the linearized model is considered as a point mass and inertia at the top of the tower. The response may also be affected by e.g. 1P loads, which are close to the wave-frequency range, but these are not considered in the simplified FWT model used in the present work. In addition, the bending moments at the tower top tend to be more non-Gaussian, and the present methodology has earlier been shown to yield less accurate fatigue damage estimates for the tower top than the rest of the support structure [14]. As the bending moments, and consequently the required structural dimensions, at the top of the tower are relatively small, this is not expected to have a large impact on the cost comparison.

Interestingly, applying all the aforementioned environmental model uncertainties results in an almost constant reduction in fatigue damage of about 65% along the length of the tower and upper part of the platform, with a corresponding change in the accumulated reliability index from 1.12 to 2.5 at the tower base. This indicates that an additional

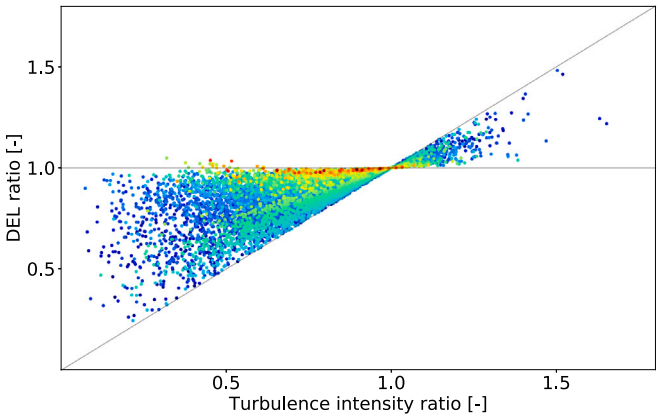

Fig. 8. DEL ratio at the tower base with stochastic and deterministic turbulence intensity. The colours indicate short-term fatigue damage magnitude, from blue (low) to red (high).

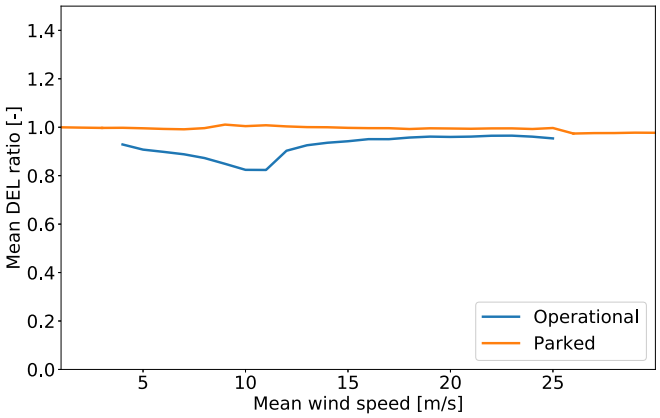

Fig. 9. Mean DEL ratio at the tower base with stochastic and deterministic turbulence intensity as a function of mean wind speed.

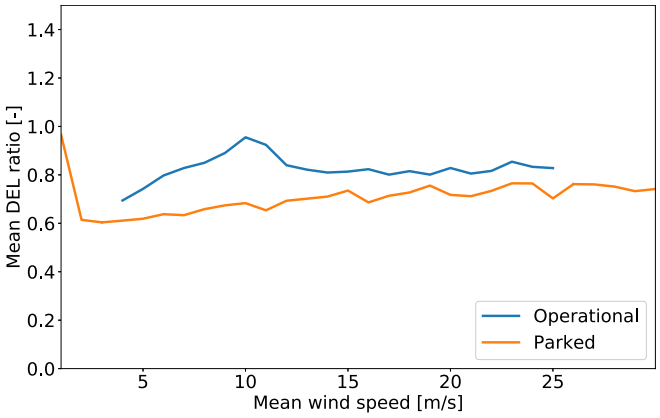

Fig. 10. Mean DEL ratio at the tower base with and without wind-wave misalignment as a function of mean wind speed.

safety factor on fatigue of about three is implicitly included when these model uncertainties are neglected for the considered system.

The effect of stochastic turbulence on the tower base DELs (i.e. damage-equivalent loads) is shown in Fig. 8. Here, each point represents a simulated wind-wave condition, and the results are given in terms of the ratios between stochastic and deterministic values. The colour of the points indicates the magnitude of the fatigue damage in the condition.

As the level of turbulence only affects the wind-induced stresses, the impact on the overall fatigue loads depends on the relative importance of wind and wave response. For a short-term condition where the stresses are completely dominated by the wave response, the DEL will be unaffected, and the points will be aligned along the horizontal grey line in the figure. In the opposite case, where the stresses are governed entirely by the wind response, the points will follow the 1:1 line along the diagonal, as the wind-induced DELs are proportional to the turbulence level for a given mean wind speed and SN curve exponent, assuming linear response [2].

While the points are quite evenly spread out between the two lines, the wind-wave conditions with the largest fatigue damage are in general associated with large waves, and consequently small relative impact of the turbulence, which places these points close to the horizontal line. In near-rated conditions, where large thrust forces on the turbine are present, the effect of turbulence is greater, as seen from the DEL ratios as a function of the mean wind speed in Fig. 9. As these conditions have high probability of occurrence and relatively large short-term fatigue damage, they have a significant impact on the long-term fatigue, and increase the overall importance of the turbulence modelling. For a parked turbine, the effects are negligible due to the dominance of wave loads.

Compared to the turbulence intensity, the effect of wind-wave misalignment follows an opposite trend. Here, the wind-wave conditions governed by wave loads are mostly affected, while small differences are observed in wind-dominated conditions. The largest differences in the tower base DELs, shown in Fig. 10, are seen for wind speeds above rated or just above cut-in, where the aerodynamic forces on the turbine are relatively small compared to the wave loads. In parked conditions, overall large reductions in stresses are observed.

7.2. Optimized designs

The optimized support structures for the base model and full environmental model after *E4* are shown in Fig. 11. The hourglass shape taken by the platform below the wave zone (from approximately 10 m below the SWL) increases the distance between the centre of buoyancy and the centre of gravity, which leads to increased pitch restoring stiffness, while the relatively large diameter at the bottom results in larger added mass and consequently a longer natural period in heave. For the upper part of the platform and intersection with the tower, the optimizer finds a balance between a small diameter, which is desirable with regards to hydrodynamic loads, and a large diameter, which (together with a small wall thickness) is the most cost-effective way to achieve the required fatigue life.

Differences in structural dimensions due to the more refined environmental model are visible both for the platform and tower. For the tower, where fatigue is seen to be the design-driving constraint along the whole length with the base model, the reduction in fatigue loads with the full environmental model results in a design with a smaller tower diameter, where the majority of the structure is fully utilized both with respect to fatigue and buckling.

Steel mass reductions in the platform occur for two reasons. Firstly, the wall thickness in the fatigue-critical wave zone is significantly reduced. Secondly, due to the lower mass of the tower and upper part of the platform, the dynamic behaviour of the system is improved, and the 15° pitch angle constraint can be satisfied with a lower draft. While the present maximum allowable pitch angle of 15° is based on common industry practice, and different values may be applied for this constraint, this will likely also be the case for other pitch angle limitations. In this particular design problem, the resulting difference in platform draft is approximately 3 m.

The resulting reductions in support structure costs with different environmental models (*E5*) are shown in Fig. 12. As expected, the largest

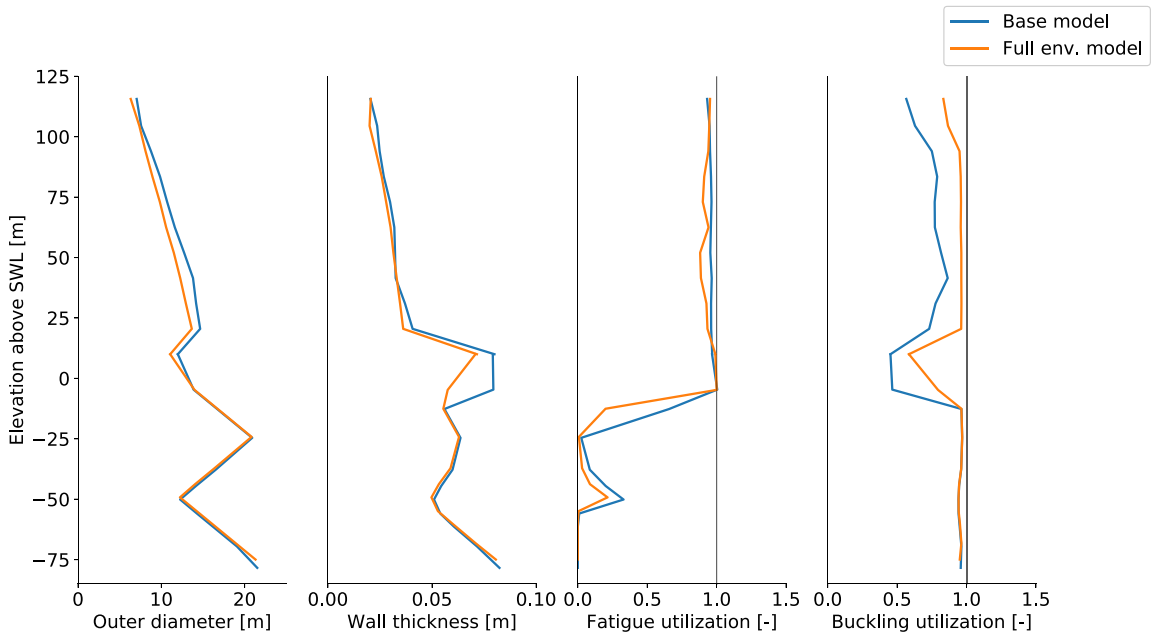

Fig. 11. Comparison of support structure dimensions and utilization factors for optimized designs.

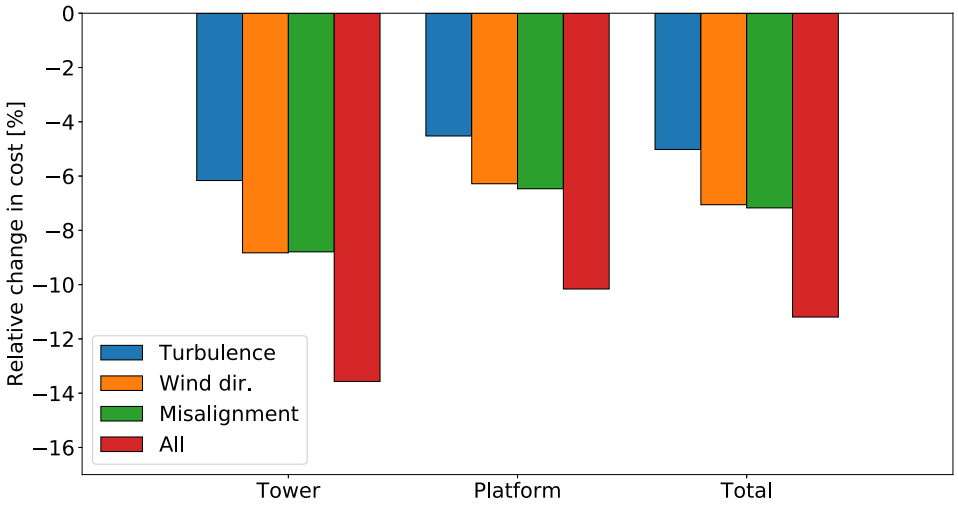

Fig. 12. Comparison of support structure costs for optimized designs with DFF1.

cost reductions are achieved for the tower, due to the fatigue-critical design. The platform design is mostly driven by the shell buckling and hydrodynamic stability constraints in the 50-year conditions, and the design costs are consequently less sensitive to the fatigue modelling.

With the present FWT concept and cost model, the platform is responsible for about 75% of the support structure costs, resulting in total cost reductions in the order of 5%–11%. These numbers are only indicative, and depend on the platform concept, considered design constraints, and the metocean conditions at the actual wind park site. As such model refinements may require more detailed in situ data and more comprehensive design calculations, project-specific assessments of the potential cost reductions are needed to find an appropriate level of detail for the environmental modelling during the design process.

7.3. DFFs and system reliability

The reliability index after 20 years of operation for optimized designs with the different DFFs from Table 4 (*I3*) is shown in Fig. 13. As expected from the design optimization results, relatively constant reliability levels are achieved along the tower length, while the larger safety factor applied for the platform results in higher reliability below the SWL. The reliability with DFF1, considering all environmental model uncertainties as described in the previous subsection, is also shown, where the more detailed environmental modelling is seen to result in a reliability level comparable to the DFF3 design.

For structures where a single component (i.e. potential fatigue crack location) dominates the failure probability, system effects for the reliability can be neglected. However, the almost constant fatigue reliability along the length of the present optimized support structure, which is a consequence of the design optimization process trying to minimize the design costs within the applied fatigue constraints at the tower and platform nodes, the system reliability must be considered. The present support structure can be modelled as a series system, where failure in one of the components results in failure of the whole structure. The system probability of failure, P_F^s, for a system with n components can

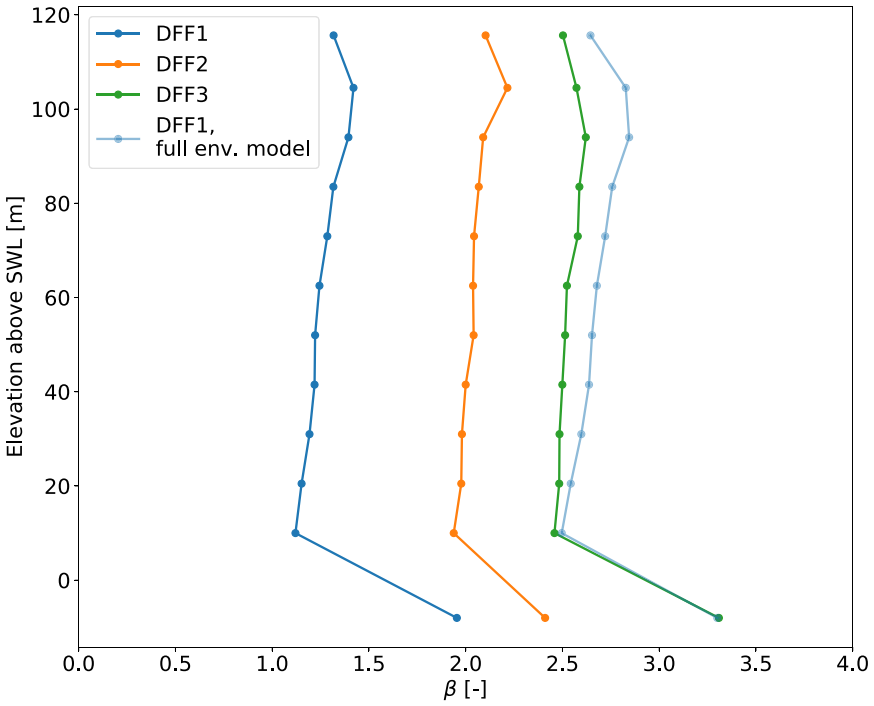

Fig. 13. Reliability index for 20 years service life.

be calculated approximately using FORM [45]:

$$P_F^s = P\left[\bigcup_{i=1}^{n} g_i \le 0\right] \approx 1 - \Phi_n(\boldsymbol{\beta}, \boldsymbol{\rho}), \tag{37}$$

where Φ_n is the n-dimensional standard normal distribution function, $\boldsymbol{\beta}$ is the vector of reliability indices for the single components, and $\boldsymbol{\rho}$ is the correlation matrix. The elements in $\boldsymbol{\rho}$ are found from $\rho_{ij} = \boldsymbol{\alpha}_i^\top \boldsymbol{\alpha}_j$, where $\boldsymbol{\alpha}$ is the unit normal vector of the linearized limit state function in standard normalized U-space:

$$g_i \approx \beta_i - \boldsymbol{\alpha}_i^\top \mathbf{u}. \tag{38}$$

Here, the fatigue strength parameters in the different components are assumed independent, while the uncertainties on the load side of the limit state function are assumed fully correlated [10]. These assumptions yield very similar correlation coefficients between the different components, and the same value is therefore applied for all non-diagonal terms in $\boldsymbol{\rho}$ for simplicity. In the last year of service, a correlation coefficient of 0.33 was obtained with DFF1.

The uncertainty in the Miner–Palmgren sum is found to dominate for the considered structure, especially in the beginning of the lifetime, which results in relatively low correlation values between the components. Similar findings were reported by Gintautas and Sørensen [10], who considered four joints in an offshore wind turbine jacket, and observed only small differences between an independent series system and a system with fully correlated load model uncertainties. The load model uncertainties (X_M and X_{SCF}) used in the present work are based on typical values from the literature, and should preferably be quantified for the specific system. Larger variation in these uncertainties would result in increased correlation between the components, and consequently less prominent system effects.

To quantify the importance of system effects on the resulting reliability, the system reliability index after 20 years of operation is shown in Fig. 14, with different number of components included in the system reliability calculations. For systems with fewer than 12 components, the most critical ones, based on the results in Fig. 13, are included.

A large reduction in reliability is observed as the number of components increases, due to the consistent failure probabilities and low correlation between the components. Based on the results presented here, the fatigue safety factor needs to be doubled for a system with eight fatigue-critical components to achieve the same accumulated reliability index in the last year of service as a support structure with a single critical component. As the number of components increases further, the curve flattens, and the impact of an additional component on the system reliability becomes smaller. For the full system considered in the present work, with 12 components contributing to to the fatigue failure probability, the additional necessary safety factor is about 2.2. This highlights the importance of system reliability in fatigue design optimization of such structures, which may have a large effect on the derived cost-optimal solutions for a given safety level. Although not considered in the present work, system effects may also affect the reliability on the wind park scale.

To assess the impact of the load model uncertainties on the correlation coefficients and consequently the system effects, the reliability index for DFF1, where the dynamic model uncertainty X_M is increased from 0.1 to 0.2, is also shown. While the larger total uncertainty translates into higher probability of failure for a single component, the increased correlation actually results in a more reliable structure with ten or more components in the series system. Although the resulting change in reliability for the total system is small, it illustrates the non-intuitive effect of increasing the load model uncertainties, which may lead to non-conservative reliability estimates for the total series system.

Relevant design guidelines [3] state that the same target safety levels are applicable for both single components and system failures, and such effects must therefore be appropriately considered in design. This can be done in a simple manner by increasing the required DFF along the entire support structure, and optimizing the structural design with consistent probabilities of failure in a large number of components.

However, the system effects observed here suggest that more cost-effective designs might be achieved if less steel-intensive parts of the structure are designed with longer fatigue life (or larger DFF), in order to reduce the system effects. To derive truly optimized fatigue designs for a given safety level, inclusion of system reliability considerations within the design optimization problem is thus required.

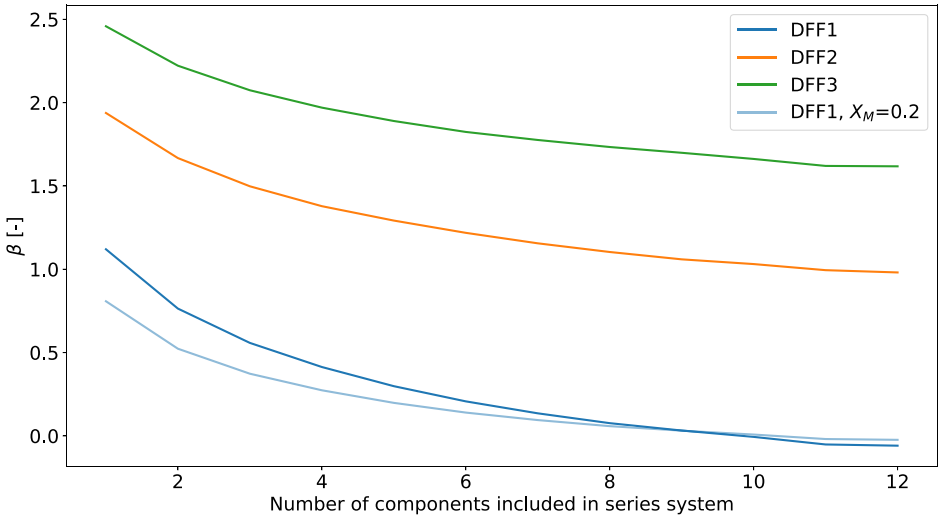

Fig. 14. System reliability index for 20 years service life as a function of components included in the series system.

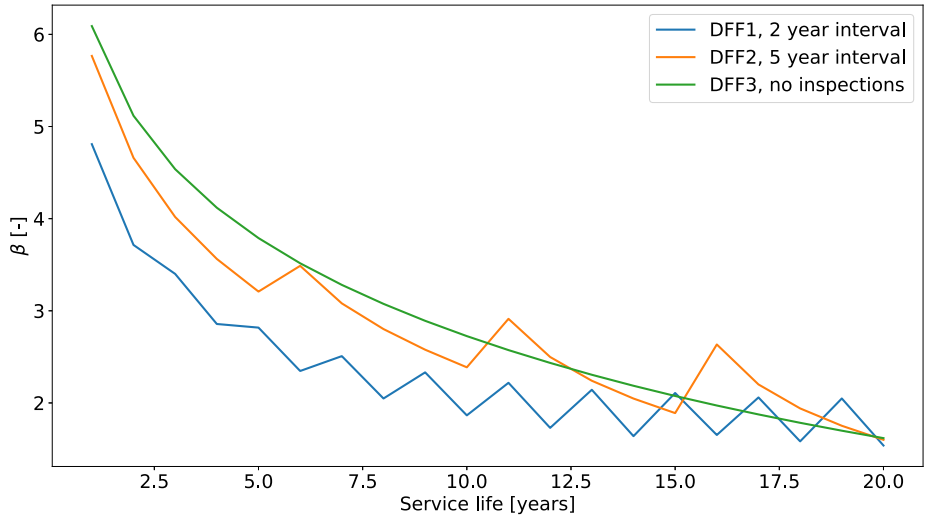

Fig. 15. System reliability index during service life, including the effect of inspections.

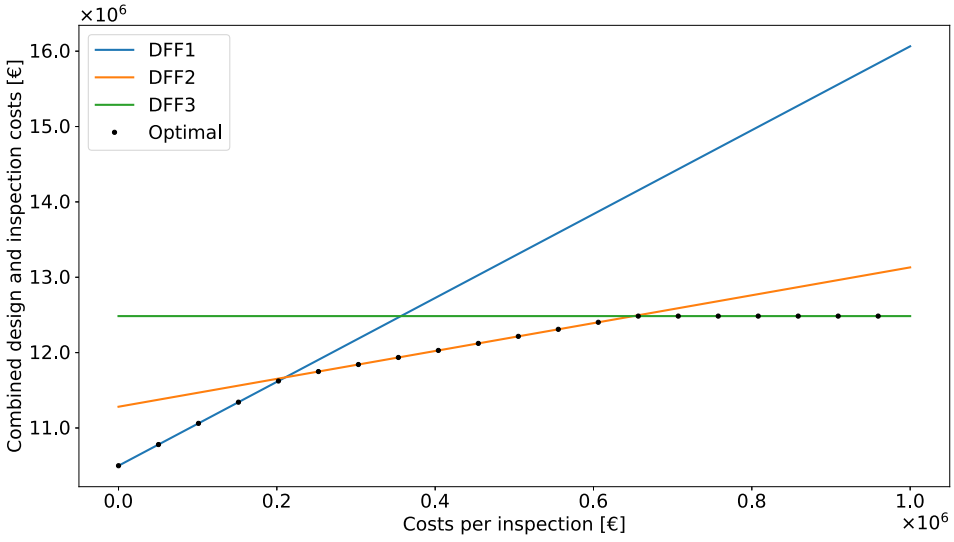

Fig. 16. Combined design and inspection costs comparison, $r = 0.05$.

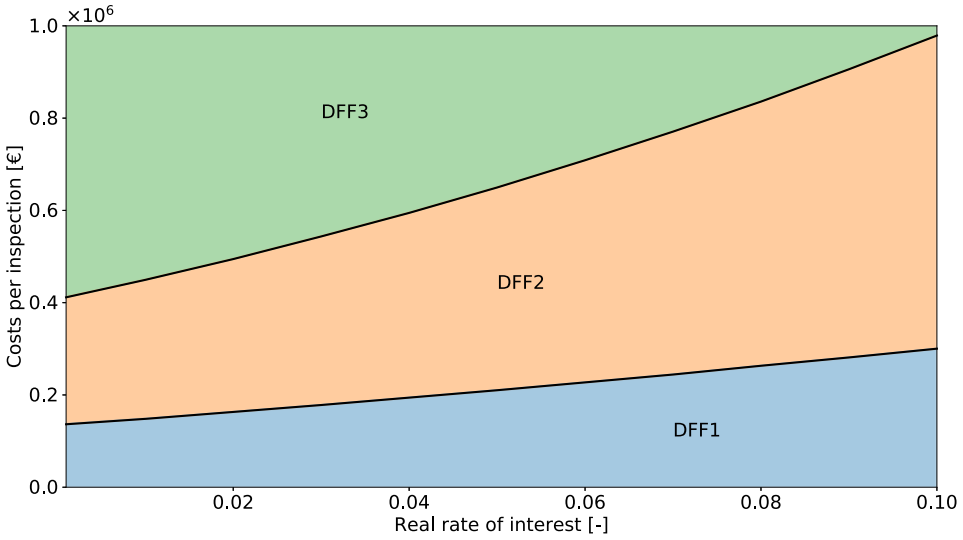

Fig. 17. Cost-optimal DFF as a function of interest rate and costs per inspection.

7.4. Trade-offs between design costs and inspection costs

An optimal risk-based inspection schedule should ideally be developed based on a given target probability of failure. However, the actual reliability level is highly dependent on the applied model uncertainties, which in the present work have been chosen solely based on typical values from the literature. Therefore, relative reliability levels are instead considered in the present work. According to DNV [46], no fatigue crack inspections are needed if a DFF of 3.0 is applied. To evaluate lifetime costs of the considered designs, necessary inspection intervals with DFF1 and DFF2 to achieve the same accumulated reliability index as DFF3 without inspections at the end of the service life are thus derived. Here, the inspections are assumed to occur with fixed intervals for each design.

Fig. 15 shows the accumulated reliability index over the service life of the wind turbine system, assuming inspections with no detection of cracks every two and five years for DFF1 and DFF2, respectively (*I4*). This corresponds to a total of nine and three inspections during the lifetime of the structure, which results in reliability indices within 5% of DFF3 without inspections after 20 years.

Based on the results in Fig. 15, trade-offs between design and inspection costs can be derived. The total expected inspection costs, C_{insp}, with k inspections is found from [42]

$$C_{\text{insp}} = \sum_{i=1}^{k} c_I \frac{1 - P_F(t_i)}{(1+r)^{t_i}}, \tag{39}$$

where c_I is the cost per inspection, and r is the real rate of interest, i.e. the nominal interest rate adjusted for inflation. As all inspections are assumed to result in no detection of cracks, repair costs are not considered.

In Fig. 16, the sum of design and inspection costs (*I5*) are shown for different values of c_I, assuming a real interest rate of 5%. In this particular case, DFF1 is the most cost-effective solution for costs per inspection lower than 210 000 €, while DFF3 is the cost-optimal design for costs of more than 650 000 € per inspection. This corresponds to about 2% and 6% of the support structure costs with DFF1, respectively.

In the present work, higher DFFs are achieved by increasing the diameter and wall thickness. Alternatively, the fatigue life could be extended by keeping the structural dimensions fixed, and instead reducing the SCF, which may be a more cost-effective option. However, the cost of improved fabrication tolerances or detail geometry is highly uncertain, and SCF reduction is therefore not considered as an option here.

As the different DFF designs result in trade-offs between current and future costs, optimal safety factors in terms of lifetime costs also depend on the interest rate. In Fig. 17, the most cost-effective DFF is shown as a function of inspection costs and real rate of interest. A doubling of r from 5% to 10% results in an increase in inspection costs at the intersections by approximately 50%.

The FWT designs in the present work have been optimized to minimize the design costs, while the effect of fatigue crack inspections has been considered subsequently. Ideally, the reliability of the structure should be included in the design process, considering costs related

Table 9
Fitting constants for wind speed at 10 m above SWL (Weibull).

Wind direction	Shape	Scale
0°	1.991	8.496
15°	1.761	6.257
30°	1.825	4.533
45°	1.957	4.324
60°	1.936	4.150
75°	1.998	4.254
90°	2.026	4.483
105°	1.909	5.274
120°	1.789	6.861
135°	2.063	8.856
150°	2.121	10.47
165°	2.419	11.31
180°	2.262	10.11
195°	2.027	8.736
210°	1.885	8.277
225°	1.926	8.713
240°	1.841	8.594
255°	1.854	8.579
270°	1.767	8.220
285°	1.696	7.619
300°	1.693	7.274
315°	1.841	7.566
330°	2.043	8.433
345°	2.270	9.575

Table 10
Fitting constants for significant wave height conditioned on wind speed (Weibull).

Wind direction	c_0, shape	c_1, shape	c_2, shape	c_0, scale	c_1, scale	c_2, scale
0°	1.811E+00	1.956E−02	1.887E+00	9.125E−01	1.552e−02	1.958E+00
15°	1.767E+00	2.122E−02	1.921E+00	9.418E−01	3.084e−02	1.692E+00
30°	8.091E+03	−8.089E+03	−6.778E−05	9.043E−01	3.686e−02	1.585E+00
45°	1.578E+00	2.181E−01	5.055E−01	4.359E+03	−4.358e+03	−7.262E−05
60°	3.801E+03	−3.799E+03	−7.664E−05	3.494E+03	−3.493e+03	−6.781E−05
75°	1.904E+00	4.263E−05	4.846E+00	2.224E+03	−2.223e+03	−8.970E−05
90°	1.874E+00	1.070E−03	3.341E+00	3.224E+03	−3.223e+03	−8.590E−05
105°	2.053E+00	2.731E−05	4.840E+00	6.111E+03	−6.110e+03	−6.512E−05
120°	2.226E+00	3.671E−06	5.275E+00	1.094E+04	−1.094e+04	−5.853E−05
135°	1.858E+00	9.106E−03	2.275E+00	8.751E−01	1.879e−02	1.797E+00
150°	1.952E+00	7.611E−03	2.309E+00	9.393E−01	1.218e−02	1.956E+00
165°	1.719E+00	4.498E−02	1.644E+00	9.666E−01	8.754e−03	2.067E+00
180°	1.682E+00	6.189E−02	1.471E+00	9.408E−01	1.311e−02	1.975E+00
195°	1.834E+00	1.922E−02	1.920E+00	9.260E−01	2.698e−02	1.793E+00
210°	2.028E+00	2.600E−03	2.720E+00	8.601E−01	5.933e−02	1.552E+00
225°	1.675E+00	5.530E−02	1.626E+00	8.882E−01	6.850e−02	1.524E+00
240°	1.541E+00	1.419E−01	1.243E+00	9.678E−01	5.919e−02	1.601E+00
255°	1.547E+00	1.252E−01	1.284E+00	8.718E−01	9.198e−02	1.457E+00
270°	1.235E+00	2.968E−01	9.501E−01	9.242E−01	7.780e−02	1.522E+00
285°	1.595E+00	8.581E−02	1.412E+00	8.658E−01	6.895e−02	1.579E+00
300°	1.753E+00	9.094E−03	2.226E+00	7.556E−01	8.405e−02	1.491E+00
315°	1.468E+00	5.111E−02	1.552E+00	7.397E−01	5.013e−02	1.669E+00
330°	1.798E+00	3.588E−03	2.447E+00	8.235E−01	1.458e−02	2.064E+00
345°	1.757E+00	1.865E−02	1.819E+00	9.965E−01	4.944e−03	2.365E+00

Table 11
Fitting constants for spectral peak period conditioned on significant wave height (Lognormal).

Wind direction	c_0, mean	c_1, mean	c_2, mean	c_0, std.dev.	c_1, std.dev.	c_2, std.dev.
0°	1.961E+00	1.165E−01	9.511E−01	4.631E−01	−1.739E−01	4.187e−01
15°	1.963E+00	1.967E−01	7.245E−01	4.563E−01	−1.941E−01	4.192e−01
30°	2.009E+00	1.818E−01	9.334E−01	4.534E−01	−2.013E−01	5.029e−01
45°	1.949E+00	2.745E−01	6.430E−01	5.680E−01	−3.243E−01	3.356e−01
60°	2.029E+00	2.000E−01	8.961E−01	5.631E−01	−3.164E−01	3.221e−01
75°	2.052E+00	1.873E−01	9.299E−01	4.218E−01	−1.712E−01	5.156e−01
90°	1.929E+00	3.247E−01	5.098E−01	4.401E−01	−1.880E−01	3.836e−01
105°	1.771E+00	4.818E−01	3.796E−01	3.889E−01	−1.314E−01	5.777e−01
120°	1.958E+00	2.784E−01	5.301E−01	4.681E−01	−2.049E−01	3.325e−01
135°	1.958E+00	2.074E−01	6.133E−01	4.873E−01	−2.023E−01	3.898e−01
150°	2.023E+00	7.857E−02	9.393E−01	4.023E−01	−9.382E−02	7.258e−01
165°	1.988E+00	5.151E−02	1.156E+00	3.996E−01	−9.105E−02	7.153e−01
180°	1.945E+00	9.234E−02	9.190E−01	3.748E−01	−6.562E−02	8.379e−01
195°	1.916E+00	1.528E−01	7.034E−01	3.481E−01	−4.982E−02	9.548e−01
210°	1.930E+00	1.519E−01	6.927E−01	3.945E−01	−1.124E−01	5.671e−01
225°	1.862E+00	2.086E−01	5.730E−01	4.073E−01	−1.384E−01	4.856e−01
240°	1.929E+00	1.498E−01	7.027E−01	3.618E−01	−1.100E−01	5.137e−01
255°	1.899E+00	1.758E−01	6.620E−01	4.031E−01	−1.527E−01	3.961e−01
270°	1.913E+00	1.725E−01	6.611E−01	4.160E−01	−1.596E−01	4.118e−01
285°	1.854E+00	2.270E−01	5.796E−01	5.044E−01	−2.466E−01	2.924e−01
300°	1.810E+00	2.704E−01	5.370E−01	4.200E−01	−1.707E−01	3.595e−01
315°	1.741E+00	3.362E−01	4.727E−01	5.805E−01	−3.102E−01	2.531e−01
330°	1.811E+00	2.204E−01	6.591E−01	5.756E−01	−2.971E−01	2.615e−01
345°	1.867E+00	1.397E−01	8.693E−01	5.039E−01	−2.077E−01	3.792e−01

to both design, maintenance, and failure. While this will significantly increase the complexity of the optimization process, benefits in terms of lifetime costs may be achieved. Further cost reductions are also possible through the use of structural health monitoring, which has been shown to improve the reliability level in various structural systems [47,48].

8. Conclusions

The impact of environmental modelling and inspection strategy on the optimal design of a 10 MW spar FWT has been assessed, based on MCS with a linearized dynamic model and a numerical design optimization procedure. Probabilistic SN and FM models were used to evaluate the fatigue reliability of the support structure, which also considered reliability updating through inspections.

Turbulence intensities based on the Weibull distribution provided by IEC [1] instead of the 90% design value had the largest impact on the fatigue loads in the upper parts of the tower, which were dominated by wind loads. The opposite effect was observed for wind-wave misalignment, which mostly affected the platform and lower parts of the tower. Inclusion of swell through a two-peak wave spectrum had negligible effect on the fatigue reliability, due to the low probability of occurrence for conditions where large differences in response were observed. The directional distribution of the wind could be considered in a simplified manner due to the axisymmetric support structure, and gave fatigue damage reductions of similar magnitude as the inclusion of wind-wave misalignment.

Including all environmental model uncertainties resulted in an almost constant reduction in fatigue damage of about two-thirds, suggesting that a case-specific safety factor of about three is included in the design when these effects are neglected. Fatigue was found to be design-driving from approximately 10 m below SWL and up to the tower top, and re-designing the support structure with the full environmental model resulted in 11% reduction of the design costs. While the majority of the cost savings were achieved directly through

Table 12
Fitting constants for relative wind-wave direction conditioned on wind speed (von Mises).

Wind direction	c_0, location	c_1, location	c_2, location	c_0, shape	c_1, shape	c_2, shape
0°	9.528E+00	4.596e−17	1.463E+01	−3.105E+00	1.806E+00	1.483e−01
15°	1.168E+01	1.856e−32	2.855E+01	−1.764E+00	2.677E−01	5.817e−01
30°	2.207E+00	1.159e−01	1.274E+00	−1.861E+00	9.642E−02	9.812e−01
45°	−5.729E+02	5.750e+02	−1.597E−04	−2.179E+00	6.622E−02	1.035e+00
60°	2.762E+00	−5.085e−01	6.913E−01	6.163E+03	−6.165E+03	−8.812e−05
75°	3.995E+00	−2.048e+00	3.517E−01	−3.587E+00	1.010E+00	6.030e−01
90°	4.302E+03	−4.302e+03	−9.125E−05	−1.801E+00	7.813E−01	7.231e−01
105°	8.349E−01	3.428e−11	1.056E+01	−2.308E+03	2.308E+03	3.682e−04
120°	1.152E+00	1.442e−07	6.980E+00	−1.550E+03	1.551E+03	7.193e−05
135°	1.386E+00	4.621e−05	4.703E+00	3.228E+00	−7.218E−01	4.519e−01
150°	2.325E+00	8.763e−08	6.744E+00	3.179E+00	−7.853E−01	4.178e−01
165°	1.961E+00	1.350e−04	4.125E+00	2.625E+00	−5.726E−01	4.506e−01
180°	2.867E+00	2.593e−07	6.362E+00	2.285E+00	−4.855E−01	4.586e−01
195°	2.935E+00	4.245e−06	5.509E+00	1.878E+00	−3.077E−01	5.563e−01
210°	3.415E+00	2.818e−05	4.825E+00	1.302E+00	−8.982E−02	8.704e−01
225°	1.695E+00	6.695e−02	2.047E+00	1.104E+00	−1.342E−01	6.732e−01
240°	3.580E+00	3.014e−03	3.186E+00	1.007E+00	−2.251E−01	4.887e−01
255°	1.852E+00	1.279e−01	1.857E+00	5.538E−01	−8.054E−02	6.629e−01
270°	2.547E+00	7.604e−02	2.040E+00	4.232E−01	−1.324E−01	4.722e−01
285°	2.179E+00	7.808e−02	2.024E+00	1.342E−01	−8.198E−02	4.442e−01
300°	2.483E+00	8.440e−02	1.858E+00	−6.534E+01	6.514E+01	8.322e−05
315°	1.490E+00	7.440e−01	1.004E+00	−7.325E+02	7.321E+02	9.251e−05
330°	−3.448E+00	5.105e+00	4.366E−01	−7.353E+00	6.682E+00	2.184e−02
345°	1.495E−01	7.373e−01	1.308E+00	−2.008E+00	1.075E+00	1.751e−01

reduction of structural dimensions due to the lower fatigue damage, the dynamic behaviour of the system also improved because of the lower mass of the tower and upper part of the platform. Consequently, the maximum platform pitch constraint could be satisfied with a lower platform draft, which was reduced by about 3 m.

Due to the applied design optimization procedure, consistent reliability levels were achieved along the tower length, which resulted in important system effects for the total structural reliability. The assumption of uncorrelated fatigue strength gave low correlation between the components, and an additional DFF of about 2.2 was found to be necessary for the considered series system with 12 welds to achieve the same reliability as a single fatigue-critical component. The system effects varied significantly with the number of components in the system and the correlation between them, and should be considered in design optimization of FWT support structures and wind farms. The required increase in the DFF due to the system effects may alter the cost-optimal design solutions for a given safety level, and suggests that less steel-intensive parts of the structure should be designed with a larger safety factor to reduce the system effects.

Trade-offs between design costs and inspection costs were derived with different DFFs. Considering fixed inspection intervals and an equal accumulated reliability index after 20 years, DFF1 was the most cost-effective design when the cost per inspection was less than 210 000 € or 2% of the CAPEX for the support structure. For more than 650 000 € per inspection, the DFF3 design with no fatigue crack inspections during the lifetime was found to be the most cost-optimal solution. These results were based on the relative reliability level between the designs, using typical model uncertainties from the literature. For an actual design process, system-specific uncertainties should be used together with a target probability of failure to determine the necessary inspection interval.

Derivation of cost-optimal fatigue designs in a lifetime perspective is a complex task which depends on a large number of uncertain parameters. The results presented here are based on a simplified dynamic FWT model, and are only valid for the specific system with the considered design constraints and assumptions. Nonetheless, the results give indications of the impact of environmental modelling, lifetime costs, and system effects for the fatigue reliability of FWT support structures, which are important in the development of cost-effective and safe design solutions.

CRediT authorship contribution statement

John Marius Hegseth: Conceptualization, Data curation, Methodology, Software, Validation, Formal analysis, Investigation, Visualization, Writing - original draft, Writing - review & editing. **Erin E. Bachynski:** Conceptualization, Methodology, Supervision, Writing - review & editing. **Bernt J. Leira:** Methodology, Supervision, Writing - review & editing.

Declaration of competing interest

The authors declare that they have no known competing financial interests or personal relationships that could have appeared to influence the work reported in this paper.

Appendix. Fitting constants for environmental model

See Tables 9–12.

References

[1] IEC. Wind turbines - part 1: design requirements. Technical report IEC 61400-1, International Electrotechnical Commission; 2005.
[2] Colone L, Natarajan A, Dimitrov N. Impact of turbulence induced loads and wave kinematic models on fatigue reliability estimates of offshore wind turbine monopiles. Ocean Eng 2018;155:295–309. http://dx.doi.org/10.1016/j.oceaneng.2018.02.045.
[3] DNV GL. Floating wind turbine structures. Technical report DNVGL-ST-0119, DNV GL; 2018.
[4] Horn J-T, Krokstad JR, Leira BJ. Impact of model uncertainties on the fatigue reliability of offshore wind turbines. Mar Struct 2019;64:174–85. http://dx.doi.org/10.1016/j.marstruc.2018.11.004.
[5] Barj L, Stewart S, Stewart GM, Lackner M, Jonkman J, Robertson A, Matha D. Wind/wave misalignment in the loads analysis of a floating offshore wind turbine. In: 32nd ASME wind energy symposium. 2014, http://dx.doi.org/10.2514/6.2014-0363.
[6] Bachynski EE, Kvittem MI, Luan C, Moan T. Wind-wave misalignment effects on floating wind turbines: motions and tower load effects. J Offshore Mech Arct Eng 2014;136. http://dx.doi.org/10.1115/1.4028028.
[7] Sørensen JD. Framework for risk-based planning of operation and maintenance for offshore wind turbines. Wind Energy 2009;12:493–506. http://dx.doi.org/10.1002/we.344.
[8] Dong W, Moan T, Gao Z. Fatigue reliability analysis of the jacket support structure for offshore wind turbine considering the effect of corrosion and inspection. Reliab Eng Syst Saf 2012;106:11–27. http://dx.doi.org/10.1016/j.ress.2012.06.011.

[9] Rangel-Ramírez JG, Sørensen JD. Risk-based inspection planning optimisation of offshore wind turbines. Struct Infrastruct Eng 2012;8(5):473–81. http://dx.doi.org/10.1080/15732479.2010.539064.

[10] Gintautas T, Sørensen JD. Reliability-based inspection planning of 20 MW offshore wind turbine jacket. Int J Offshore Polar Eng 2018;28(3):272–9. http://dx.doi.org/10.17736/ijope.2018.jl53.

[11] Márquez-Domínguez S, Sørensen JD. Fatigue reliability and calibration of fatigue design factors for offshore wind turbines. Energies 2012;5:1816–34. http://dx.doi.org/10.3390/en5061816.

[12] Velarde J, Kramhøft C, Sørensen JD, Zorzi G. Fatigue reliability of large monopiles for offshore wind turbines. Int J Fatigue 2020;134. http://dx.doi.org/10.1016/j.ijfatigue.2020.105487.

[13] Ziegler L, Rhomberg M, Muskulus M. Design optimization with genetic algorithms: how does steel mass increase if offshore wind monopiles are designed for a longer service life? J Phys Conf Ser 2018;1104. http://dx.doi.org/10.1088/1742-6596/1104/1/012014.

[14] Hegseth JM, Bachynski EE, Martins JRRA. Integrated design optimization of spar floating wind turbines. Mar Struct 2020;72:102771. http://dx.doi.org/10.1016/j.marstruc.2020.102771.

[15] Bak C, Zahle F, Bitsche R, Yde A, Henriksen LC, Natarajan A, Hansen MH. Description of the DTU 10 MW reference wind turbine. Technical report DTU Wind Energy Report-I-0092, DTU Wind Energy; 2013.

[16] Hegseth JM, Bachynski EE. A semi-analytical frequency domain model for efficient design evaluation of spar floating wind turbines. Mar Struct 2019;64:186–210. http://dx.doi.org/10.1016/j.marstruc.2018.10.015.

[17] MacCamy RC, Fuchs RA. Wave forces on piles: a diffraction theory. Technical report technical memorandum 69, Beach Erosion Board; Corps of Engineers; 1954.

[18] Lackner M. Controlling platform motions and reducing blade loads for floating wind turbines. Wind Eng 2009;33(6):541–53. http://dx.doi.org/10.1260/0309-524X.33.6.541.

[19] Hegseth JM, Bachynski EE, Martins JRRA. Design optimization of spar floating wind turbines considering different control strategies. J Phys Conf Ser 2020;1669:012010.

[20] Naess A, Moan T. Stochastic dynamics of marine structures. Cambridge University Press; 2013.

[21] DNV GL. Loads and site conditions for wind turbines. Technical report DNVGL-ST-0437, DNV GL; 2016.

[22] Dirlik T. Application of computers in fatigue analysis [Ph.D. thesis], University of Warwick; 1985.

[23] Lotsberg I. Fatigue design of marine structures. Cambridge University Press; 2016.

[24] Reistad M, Breivik Ø, Haakenstad H, Aarnes OJ, Furevik BR, Bidlot J-R. A high-resolution hindcast of wind and waves for the North Sea, the Norwegian Sea, and the Barents Sea. J Geophys Res Oceans 2011;116(5):1–18. http://dx.doi.org/10.1029/2010JC006402.

[25] IEC. Wind turbines - part 3: design requirements for offshore wind turbines. Technical report IEC 61400-3, International Electrotechnical Commission; 2009.

[26] Horn J-T, Bitner-Gregersen E, Krokstad JR, Leira BJ, Amdahl J. A new combination of conditional environmental distributions. Appl Ocean Res 2018;73:17–26. http://dx.doi.org/10.1016/j.apor.2018.01.010.

[27] Gray JS, Hwang JT, Martins JRRA, Moore KT, Naylor BA. OpenMDAO: an open-source framework for multidisciplinary design, analysis, and optimization. Struct Multidiscip Optim 2019;59:1075–104. http://dx.doi.org/10.1007/s00158-019-02211-z.

[28] Gill PE, Murray W, Saunders MA. SNOPT: an SQP slgorithm for large-scale constrained optimization. SIAM J Optim 2002;12(4):979–1006. http://dx.doi.org/10.1137/S0036144504446096.

[29] Perez RE, Jansen PW, Martins JRRA. pyOpt: A python-based object-oriented framework for nonlinear constrained optimization. Struct Multidiscip Optim 2012;45(1):101–18. http://dx.doi.org/10.1007/s00158-011-0666-3.

[30] Farkas J, Jármai K. Optimum design of steel structures. Springer; 2013.

[31] Teillant B, Krügel K, Guérinel M, Vicente M, Debruyne Y, Malerba F, Gradowski M, Roveda S, Neumann F, Noorloos HV, Schuitema R, Gomes R, Henriques J, Gato L, Combourieu A, Neau A, Borgarino B, Doussal J-C, Philippe M, Moretti G, Fontana M. WETFEET – wave energy transition to future by evolution of engineering and technology D2.3: engineering challenges related to full scale and large deployment implementation of the proposed breakthroughs. Technical report, WavEC Offshore Renewables; 2016.

[32] DNV GL. Fatigue design of offshore steel structures. Technical report DNVGL-RP-C203, DNV GL; 2019.

[33] DNV. Design of floating wind turbine structures. Technical report DNV-OS-J103, DNV; 2013.

[34] European Committee for Standardization. Eurocode 3: design of steel structures, part 1-6: strength and stability of shell structures. Technical report EN 1993-1-6: 2007, European Committee for Standardization; 2007.

[35] DNV GL. Buckling strength of shells. Technical report DNVGL-RP-C202, DNV GL; 2019.

[36] Kreisselmeier G, Steinhauser R. Systematic control design by optimizing a vector performance index. In: International federation of active controls symposium on computer-aided design of control systems. 1979, http://dx.doi.org/10.1016/s1474-6670(17)65584-8.

[37] Madsen HO, Krenk S, Lind NC. Methods of structural safety. Prentice-Hall; 1986.

[38] Tvedt L. Proban - probabilistic analysis. Struct Saf 2006;28(1–2):150–63. http://dx.doi.org/10.1016/j.strusafe.2005.03.003.

[39] Horn J-T, Leira BJ. Fatigue reliability assessment of offshore wind turbines with stochastic availability. Reliab Eng Syst Saf 2019;191:106550. http://dx.doi.org/10.1016/j.ress.2019.106550.

[40] DNV GL. Probabilistic methods for planning of inspection for fatigue cracks in offshore structures. Technical report DNVGL-RP-C210, DNV GL; 2019.

[41] Kirkemo F. Applications of probabilistic fracture mechanics to offshore structures. Appl Mech Rev 1988;41(2):61–84. http://dx.doi.org/10.1115/1.3151882.

[42] Madsen HO, Sørensen JD, Olesen R. Optimal inspection planning for fatigue damage of offshore structures. In: Proceedings of ICOSSAR'89, the 5th international conference on structural safety and reliability, 1989.

[43] Melchers RE, Beck AT. Structural reliability analysis and prediction. 3rd ed.. Wiley; 2018.

[44] Torsethaugen K, Haver S. Simplified double peak spectral model for ocean waves. In: Proceedings of the fourteenth (2004) international ocean and polar engineering conference, 2004.

[45] Moan T, Song R. Implications of inspection updating on system fatigue reliability of offshore structures. J Offshore Mech Arct Eng 2000;122:173–80. http://dx.doi.org/10.1115/1.1286601.

[46] DNV GL. Support structures for wind turbines. Technical report DNVGL-ST-0126, DNV GL; 2018.

[47] Thöns S, Schneider R, Faber MH. Quantification of the value of structural health monitoring information for fatigue deteriorating structural systems. In: 12th International conference on applications of statistics and probability in civil engineering, 2015.

[48] Leira BJ. Reliability updating based on monitoring of structural response parameters. Reliab Eng Syst Saf 2016;155:212–23. http://dx.doi.org/10.1016/j.ress.2016.07.006.